Mechanisms of Low Cloud–Climate Feedback in Idealized Single-Column Simulations with the Community Atmospheric Model, Version 3 (CAM3)

MINGHUA ZHANG

School of Marine and Atmospheric Sciences, Stony Brook University, Stony Brook, New York

CHRISTOPHER BRETHERTON

Departments of Atmospheric Sciences and Applied Mathematics, University of Washington, Seattle, Washington

ABSTRACT

This study investigates the physical mechanism of low cloud feedback in the Community Atmospheric Model, version 3 (CAM3) through idealized single-column model (SCM) experiments over the subtropical eastern oceans. Negative cloud feedback is simulated from stratus and stratocumulus that is consistent with previous diagnostics of cloud feedbacks in CAM3 and its predecessor versions. The feedback occurs through the interaction of a suite of parameterized processes rather than from any single process. It is caused by the larger amount of in-cloud liquid water in stratus clouds from convective sources, and longer lifetimes of these clouds in a warmer climate through their interaction with boundary layer turbulence. Thermodynamic effects are found to dominate the negative cloud feedback in the model. The dynamic effect of weaker subsidence in a warmer climate also contributes to the negative cloud feedback, but with about one-quarter of the magnitude of the thermodynamic effect, owing to increased low-level convection in a warmer climate.

1. Introduction

Cloud–climate feedback plays a significant role in determining the sensitivity of general circulation models (GCMs) (e.g., Cess et al. 1990). Several recent papers have reviewed progresses made in the last 20 years on this subject (Zhang 2004; Stephens 2005; Bony et al. 2006; Randall et al. 2007). As concluded in the most recent Intergovernmental Panel on Climate Change (IPCC) Assessment Report: "Cloud feedbacks remain the largest source of uncertainty" in determining the sensitivity of the current climate models. There is little evidence of convergence of the models in simulating cloud feedbacks at the present time (e.g., Bretherton et al. 2004; Miura et al. 2005; Soden and Held 2006; Kiehl et al. 2006; Webb et al. 2006; Wyatt et al. 2006b).

A prerequisite to improve our confidence on the cloud feedback of a model is the understanding of its physical mechanism. Such an understanding is also im-

portant to guide the improvement of physical parameterizations of the model. Several hypotheses have been proposed in the past. For example, Somerville and Remer (1984) suggested that in a warmer climate, low clouds tend to contain more liquid water that reflects solar radiation, which constitutes a negative cloud feedback. Wetherald and Manabe (1988) along with several other studies (e.g., Hansen et al. 1984) suggested that warmer climate is accompanied by higher altitude of convection, and thus more clouds near the tropopause that give rise to a positive longwave cloud feedback. Other studies (e.g., Senior and Mitchell 1993, 1996; Le Treut et al. 1994; Del Genio et al. 2005) have shown great sensitivities of cloud feedbacks to the cloud microphysical scheme in the models. Several authors have used box models to study low cloud feedback mechanisms (e.g., Miller 1997; Larson et al. 1999; Clement and Seager 1999). Recently, Caldwell and Bretherton (2008) used a stratocumulus-capped mixed-layer model to report a negative cloud feedback. They included cloud-top entrainment and drizzle parameterizations, as well as the interaction of the cloud-induced radiative cooling with dynamical circulations. In their model, the negative cloud feedback was due to the increase of

---

Corresponding author address: Minghua Zhang, School of Marine and Atmospheric Sciences, Stony Brook University, Stony Brook, NY 11794-5000.
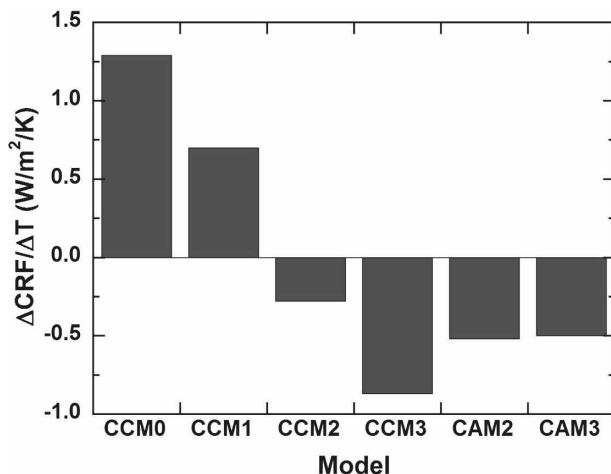E-mail: mzhang@notes.cc.sunysb.edu

FIG. 1. History of diagnosed cloud feedbacks in the CAM3 and its predecessors. All numbers are diagnosed from a surrogate climate change of SST increase by 2 K.

cloud liquid water associated with thickening of clouds in a warmer climate. While these studies have all provided useful insights about the response of clouds to a climate change, the knowledge on the mechanism of cloud feedbacks is still very limited either because of the difficulties in fully understanding the behavior of a GCM or because of the simplicity of the cloud models used.

The purpose of this study is to examine the physical mechanisms of cloud feedback in the CAM3. Figure 1 shows the history of the diagnosed cloud feedbacks in this model and its predecessor versions (Zhang 2004). The cloud feedback is calculated by using the change of cloud radiative forcing (CRF) per unit degree of surface temperature increase in a surrogate climate change (Cess et al. 1990). Soden et al. (2004) argued that this measure is not necessarily equivalent to a cloud feedback. Since the magnitude of cloud feedback depends on the definition of the reference system without feedback, the variation of cloud forcing can be considered as the cloud feedback if the reference system is defined as the clear-sky atmosphere. Zhang et al. (1994) and Soden et al. (2004) all showed that this is still a good measure of the impact of clouds on model climate sensitivity (Zhang et al. 1994). Therefore, we use this definition of cloud feedback in this study. It is intended to describe the impact of varying clouds on the radiative budget of the earth–atmosphere column. Figure 1 shows that, since version 2 of the Community Climate Model (CCM2), cloud feedback has been negative in the model, despite the many changes introduced in version 3 (CCM3), the Community Atmosphere Model, versions 2 (CAM2) and 3 (CAM3) (Hack et al. 1993; Kiehl et al. 1998; Kiehl and Gent 2004; Collins et al.

2006). The negative cloud feedback in CAM is in contrast to the positive cloud feedback in many other models. As a consequence, its projection of global warming in response to a doubling of CO_2 in the atmosphere has been at the low end of those in various multimodel comparisons (Solomon et al. 2007). It has been known that the primary reason for the negative cloud feedback is a predicted increase of low clouds (Bretherton et al. 2004; Wyant et al. 2006a). This is consistent with findings in Bony and Dufresne (2005) that highlighted the role of low clouds in climate feedback. The exact reason why low clouds are increased is not clear.

To understand the physical processes that might be responsible for low cloud feedbacks in the CAM3, we designed idealized experiments to simplify the model dynamics. The idealized experiments are intended to mimic the subsidence regimes over the subtropical eastern oceans where stratus and stratocumulus dominate. We use the single-column version of the model to decipher the feedback mechanisms. Even though these mechanisms are not necessarily the same as in a climate change of the GCM, they offer a unique perspective to the internal workings of the model physics.

One finding of this study is that our idealized setup of climate change experiments reproduced the negative cloud feedback of the parent GCM. A second major finding is that cloud feedback in the model is caused by the interaction of many individual physical parameterization components rather than a single process. In a nutshell, the negative cloud feedback is due to both increased in-cloud liquid water of stratiform clouds from convective sources and longer duration of the convective life cycle. The longer life cycle is traced to the smaller sensitivity of cloud water than that of precipitation to a warmer climate.

The paper is organized as follows. Section 2 presents the design of the idealized experiments. It describes the large-scale dynamical conditions in both the control and perturbed simulations. Section 3 reports how low clouds are maintained and how they respond to warming in the CAM3 under the idealized setup. The last section contains a summary and discussion.

2. Experimental setup

a. Forcing data

The large-scale dynamic forcing is designed to emulate the advective tendencies of temperature and water vapor with the following two conditions in mind: 1) they should represent the large-scale environmental conditions of low clouds in the eastern Pacific as in the GCMs and 2) they can be used for simulations representing both the present and a warmer climate. In
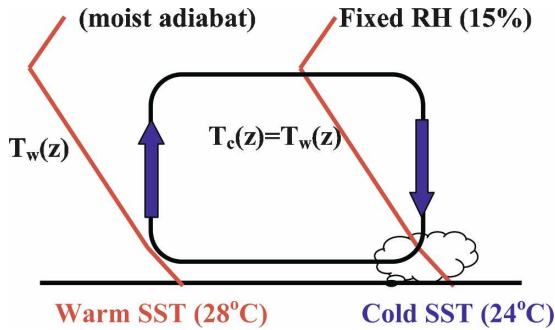
FIG. 2. Schematics of the experimental setup. The cold tongue refers to SST in the eastern subtropical Pacific. The SST values for the control simulation are shown in parentheses.

GCMs, these large-scale forcing fields vary in space and time. In our setup, we purposely keep the forcing data invariant with time to simplify the problem.

Figure 2 describes the schematic setup of the large-scale forcing fields. We start from two sea surface temperatures (SSTs) that represent a warm pool (T_w) and a cold pool (T_c) that should be considered as the subtropical eastern oceans. In the control simulation T_w is specified as 28°C and T_c as 24°C. As in Caldwell and Bretherton (2008), surface air temperature is assumed to be 1°C colder than the SST. The atmospheric temperature over the warm pool $T(z)$ is then specified by adiabatically lifting a surface air parcel with $T = 27$°C and a relative humidity of 75% at 1000 mb. This yields a temperature profile that approximately matches the shape of the mean profile of $T(z)$ during Tropical Ocean and Global Atmosphere Coupled Ocean–Atmosphere Response Experiment (TOGA COARE), which are all shown in Fig. 3a. Temperature above 200 mb is assumed to be that of TOGA COARE. The atmospheric temperature throughout the troposphere over the cold pool is assumed to be the same as that over the warm pool for the derivation of the forcing data, in which no boundary layer is assumed to exist. This free-atmosphere temperature profile is justified by the small horizontal temperature gradient in the tropics. This assumption is only used to derive the approximate subsidence rate over the cold pool and should not be used to rule out the existence of horizontal forcing by temperature advection of the idealized model simulation.

The profiles of wind components over the cold pool are taken from the mean winds at the middle point of the European Cloud System Experiment (EUROCS) cross section in the eastern subtropical Pacific from a GCM simulation (17°N, 147°W). Figure 3b shows the vertical profiles of winds for the control simulation. Water vapor over the cold SST is specified by using a fixed relative humidity of 15%, which is close to the

minimum free-atmosphere mean relative humidity at the EUROCS location in the GCM and in the European Centre for Medium-Range Weather Forecasts (ECMWF) analysis. Above the tropopause, a constant mixing ratio of 4 ppmv is used.

For the perturbed experiments representing a warmer climate, SSTs (T_w and T_c) are uniformly raised by 2° as in Cess et al. (1990). This is accompanied by corresponding moist-adiabatic changes in the vertical profiles of temperature over the warm pool and thus over the cold pool. As in the control experiment, the moist adiabat is only used up to 200 mb. At 200 mb, a temperature excess compared to the TOGA COARE sounding is calculated. Between 200 and 100 mb, the temperature excess is linearly ramped down to zero, and this excess is added to the TOGA COARE sounding to obtain the temperature profile in the stratosphere.

Based on the cold pool SST and the profiles of temperature and water vapor, we derive the atmospheric subsidence and advective tendencies in three steps. First, the profile of net radiative cooling in the atmosphere is calculated. The top-of-the-atmosphere (TOA) incoming solar radiation is specified as the mean value at 20°N under equinox condition, which is 408.7 W m^{-2} corresponding to a cosine zenith angle of 0.299. Diurnal variation is not included. The surface albedo is fixed as 0.1. The ozone profile is taken from the standard atmosphere for summer middle latitude conditions (McClatchey et al. 1972). The CAM3 radiative transfer model is used for the calculation of the heating rate, which is shown in Fig. 4a for both the control case (solid line) and the perturbed case (dashed line). The maximum radiative cooling occurs near the surface due to the large concentration of water vapor and at the maximum emission levels at around 300 mb. Above 150 mb there is radiative warming. Within 50 mb of the tropopause, at around 100 mb, the magnitudes of warming from longwave and shortwave are comparable to each other. Above this layer, the shortwave warming due to ozone absorption of solar radiation dominates. This warming is expected to offset the cooling from the rising motion of the Brewer–Dobson circulation in the real atmosphere.

In the second step, we calculate the atmospheric subsidence over the cold SST based on the radiative cooling rate. A local balance between subsidence warming and radiative cooling would give the following pressure vertical velocity:

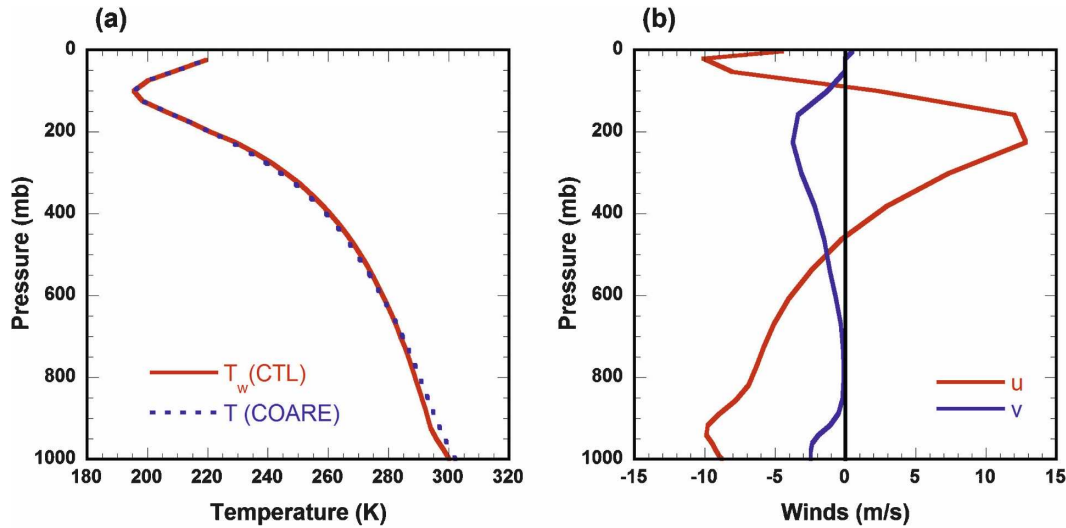$$\omega^* = -\frac{Q_R(p)}{C_p} \Big/ \left(\frac{\partial \theta_0}{\partial p}\right), \tag{1}$$

FIG. 3. (a) Temperature profile (T_w) specified in the control simulation and its comparison with the mean profile from TOGA COARE. (b) Profiles of specified wind components.

where Q_R is the radiative heating rate, θ_0 is the potential temperature, and C_P is the specific heat of air for fixed pressure. This subsidence rate would peak in the upper and lower troposphere as the radiative cooling rate does. Therefore, instead of using the local balance equation of (1), we assume that the vertically integrated large-scale transport of heat balances the total atmospheric radiative cooling in the absence of a boundary layer, and that the subsidence rate follows a specified shape:

$$\omega_0(p) = \begin{cases} A \cos^{(1/3)}[(p_{max} - p)/(p_{max} - 150) \times \pi/2], & 150 \text{ mb} < p < p_{max} \\ A \cos[(p - p_{max})/(1000 - p_{max}) \times \pi/2], & p_{max} < p < 1000 \text{ mb} \end{cases} \tag{2}$$

so that

$$\int_{\theta_{0\_1000mb}}^{\theta_{0\_150mb}} \omega_0 \, d\theta_0 = \int_{\theta_{0\_1000mb}}^{\theta_{0\_150mb}} \omega^* \, d\theta_0. \tag{3}$$

The peak subsidence level p_{max} separates regions of large-scale convergence in the upper troposphere from regions of divergence in the lower atmosphere. It is specified as 800 mb in this study. The shape function and the peak level p_{max} are chosen to approximate the subsidence in the GCM at the EUROCS middle point. Above 150 mb, where there is radiative warming, the vertical velocity ω_0 is set to zero. Figure 4b shows the derived subsidence rate in both the control climate (solid black) and warmer climate (solid red). The subsidence rates at the EUROCS location in the CAM3 and in the ECMWF operational analysis for July 2003 (courtesy of M. Kohler of ECMWF) are also shown in the figure. It is seen that the derived subsidence rates capture the main characteristics of those in both the GCM and the operational analysis.

Note that for the perturbed case, the atmospheric radiative cooling rate is larger only at the maximum emission level (Fig. 4a). In the middle and lower troposphere, the radiative cooling differs very little between the two cases owing to the greenhouse effect of water vapor. Because moist adiabats have smaller lapse rate in a warmer climate, the subsidence rate is weaker in the warmer climate (Fig. 4b). This reduction of subsidence has been related to the weakening of the Walker circulation (Zhang and Song 2006; Vecchi et al. 2006) and was shown as important to the cloud feedback processes in a mixed-layer model study by Caldwell and Bretherton (2008).

In the last step, we calculate the vertical advective tendencies of temperature and water vapor by using their prescribed profiles and the subsidence rate and the horizontal temperature tendency as a residual of the subsidence warming and radiative cooling:

$$-(\mathbf{V} \cdot \boldsymbol{\nabla}\theta)_{LS0} = \omega_0 \frac{\partial \theta_0}{\partial p} - \frac{Q_R}{c_p}. \tag{4}$$

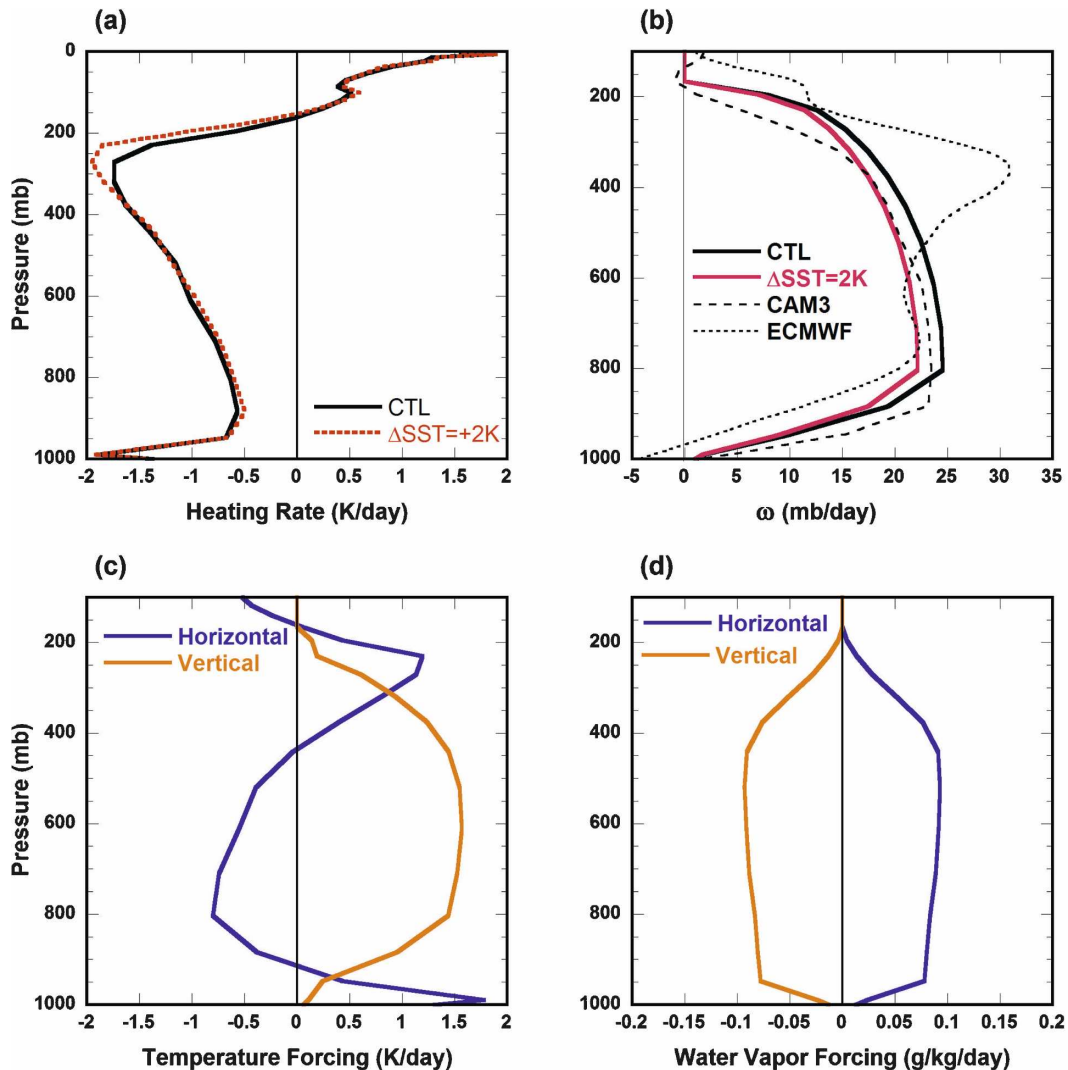The horizontal moisture tendency is specified to balance the subsidence drying:

FIG. 4. (a) Rate of radiative cooling in the control and warm climate. (b) Calculated rate of subsidence for the control and warm climate. Also plotted are the mean subsidence rates from climatological CAM3 simulations and from ECMWF operational analysis for July 2003 at (17°N, 147°W). Large-scale horizontal and vertical advective forcing of (c) temperature and (d) water vapor in the control simulation.

$$-(\mathbf{V} \cdot \boldsymbol{\nabla} q)_{LS0} = \omega_0 \frac{\partial q_0}{\partial p} \,. \qquad (5)$$

Figure 4c shows the horizontal (blue) and vertical (red) forcing of temperature for the control case. Figure 4d shows the corresponding tendencies for water vapor. The qualitative features of subsidence warming and drying, and the horizontal advective cooling and moistening in the middle troposphere, are all similar to those in the CAM3 climatological simulations. Near the surface, however, because of the interactive nature of the boundary layer with dynamical circulations, the horizontal forcing terms in the GCM have more complicated structures. Large-scale forcing for the warmer cli-

mate is derived using the same procedure. We note that the assumptions on the local thermodynamic balance of Eq. (1) and the free atmospheric temperature over the cold pool are used only to estimate the subsidence rate that is responsive to the SST. The specified horizontal forcing of temperature and moisture is intended to prevent the model from drifting in the free atmosphere without a boundary layer in the course of integration in this idealized setup.

Caldwell and Bretherton (2008) employed a similar procedure to derive the large-scale forcing in their study of the stratocumulus-capped mixed layer except that they prescribed the horizontal advection of temperature and then used the energy balance at each

height to derive the subsidence for a warmer climate. In their formulation, the vertical motion also responds to the boundary-layer-induced diabatic heating perturbation due to radiative and turbulent fluxes, an effect that we do not include here because it adds complexity to the model.

b. Description of experiments

The single column model for temperature and water vapor can be schematically written as

$$\left(\frac{\partial \theta}{\partial t}\right) = -(\mathbf{V} \cdot \boldsymbol{\nabla}\theta)_{LS0} - \omega_0 \frac{\partial \theta}{\partial p} + \left(\frac{\partial \theta}{\partial t}\right)_{\text{phys}}, \quad (6)$$

$$\left(\frac{\partial q}{\partial t}\right) = -(\mathbf{V} \cdot \boldsymbol{\nabla}q)_{LS0} - \omega_0 \frac{\partial q}{\partial p} + \left(\frac{\partial q}{\partial t}\right)_{\text{phys}}, \quad (7)$$

where the last term in the two equations represent tendencies from all physical parameterizations. Vertical advection in the model is calculated using the profiles of temperature and moisture in the simulations. In the absence of any heating or moisture sources other than radiation, the model has an equilibrium solution of T_0 and q_0 under subsidence ω_0 with the specified values of the horizontal forcing. The values of the actual forcing would then be exactly the same as described in the previous section and in Fig. 4. Since in the model simulation a boundary layer would develop, the vertical tendencies in (6)–(7) would differ from those in (4) and (5) with much larger magnitude at the top of the boundary layer. The interactive vertical temperature advection prevents the simulation above the boundary layer from drifting due to the additional radiative cooling from the boundary layer clouds. Equations (4) and (5), however, are necessary to calculate the fixed horizontal forcing.

An upstream difference scheme is used for the integration of the vertical gradients in (6)–(7) to ensure numerical stability. In addition, since the moist adiabats near the tropopause are close to the dry adiabats, to avoid shallow convection in the upper tropopause, we relax the temperature and water vapor to the initial profiles above 300 mb.

3. Results

a. Clouds in the control simulation

After a spin up of 10 days, the model reaches a quasi-steady state. It simulates low stratus and stratocumulus clouds, as intended. Figure 5a shows the time–height distribution of cloud amount for 70 days. Instead of being a true steady state, the simulated fields vary quasi periodically with a period of slightly less than a day.

Figure 5b shows a segment of the time series of the column cloud amount for total clouds and convective clouds. The cloud amount varies from an overcast condition to about 30% in a cycle. Stratiform clouds dominant the total cloud amount. Convective clouds are present at all times. The variation of total clouds has a small lag relative to the convective clouds.

The dashed line in Fig. 5c shows the time variation of the column-integrated total cloud liquid water path. It closely follows the total cloud amount. The shortwave (SW) and longwave (LW) cloud forcing at the TOA track the cloud liquid water path. In the figure, we plot −SW CRF for easy viewing. The magnitude of SW CRF is much larger than the LW CRF due to the low altitudes of these clouds.

Two questions are important for later discussions on the response of clouds to a climate warming: How are clouds maintained in the control simulation? What determines the period of the cloud variations?

In the CAM3, cloud amount is calculated based on convective mass fluxes (convective clouds) and relative humidity (stratiform clouds) as well as stability through the Klein and Hartmann (1993) relationship. The later case did not occur in the present simulation. The total cloud in a layer is the sum of the convective and stratiform clouds with an upper limit of 100%. The CAM3 sequentially calls two convection schemes. The first is the Zhang and McFarlane scheme (1995), designed for penetrative convection, and the second is the shallow convection scheme of Hack (1994). These will be referred to as the Zhang–McFarlane (ZM) and Hack (HK) schemes in this paper. Like the relaxed Arakawa–Schubert scheme (Moorthi and Suarez 1992; GFDL Global Atmospheric Model Development Team 2004), the ZM scheme calculates the convective mixing when air parcels originating from the lowest model layer are conditionally unstable. In contrast, the HK scheme becomes active when an air parcel in an adjacent layer immediately below, but above the surface layer, is unstable relative to a given model. Because the simulated clouds (Fig. 5a) are concentrated in one single model layer at ~900 mb, we use Fig. 6a to show the cloud amount at 900 mb from the stratiform scheme and the two convection schemes, both of which are active during a cycle. Consistent with the cloud amount for the whole column, stratiform cloud is the dominant cloud type when averaged over a cycle.

Figure 6b shows the tendencies of water vapor at 900 mb from the different model components including the ZM and HK convection schemes, the stratiform cloud condensation scheme, boundary layer turbulence, and large-scale forcing. The thin blue line shows the total tendency. It is seen that, when the ZM scheme is active
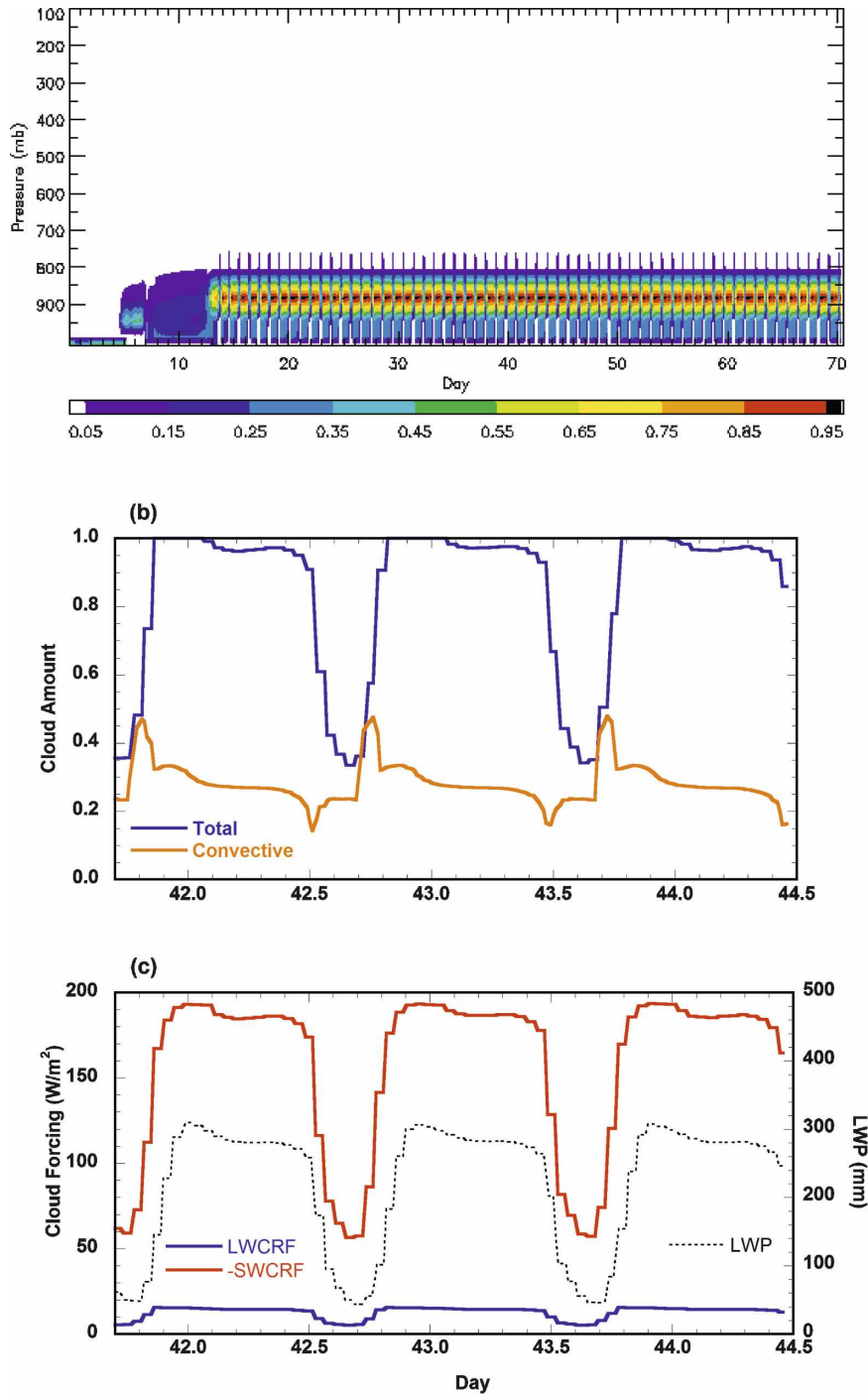
FIG. 5. (a) Time–pressure cross section of simulated cloud amount. (b) A time segment of the total and convective cloud amount for the atmospheric column. (c) Column-integrated cloud liquid path and cloud forcing.

(the red line), it acts as the largest source of water vapor for the layer. This is balanced by large-scale drying (dashed green) and stratiform condensation (cyan). The ZM scheme does not perpetuate itself however.

When it is deactivated, stratiform cloud amount decreases significantly (Fig. 6a), and the HK scheme becomes active. Unlike the ZM scheme, the HK scheme acts as a moisture sink to dry the layer (Fig. 6b, dashed
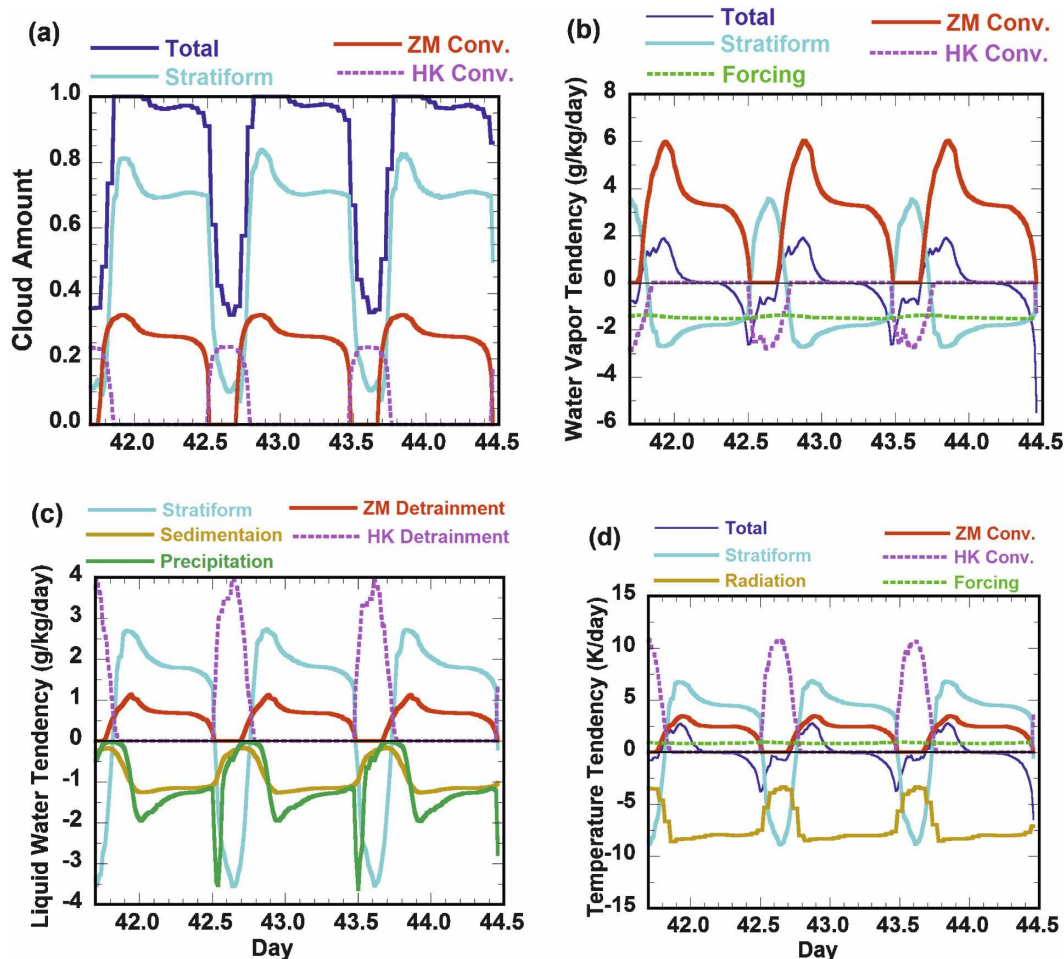
FIG. 6. Time series of simulated variables from the various components of physical parameterizations in the 900-mb layer: (a) cloud amount, (b) water vapor tendency, (c) liquid water tendency, and (d) temperature tendency.

magenta line). This is, however, largely offset by the evaporation of existing and newly detrained liquid water through the stratiform cloud scheme.

The overall moisture budget in the cloud layer is therefore between the source of convective transport by the ZM scheme and the sinks due to stratiform condensation and large-scale drying. The HK scheme also contributed to drying. But it is offset to a large degree by the evaporation of its detrained liquid water. If we consider the HK scheme as entraining dry air into the cloud layer, the water vapor budget in the simulation shares some features of the classical conceptual model in which convective moistening is balanced by large-scale drying and entrainment. This drying evaporates cloud water.

Figure 6c shows the time series of the liquid water budget in the cloud layer. When the ZM scheme is active, stratiform condensation (cyan line) constitutes the largest source of cloud liquid water. It is more than twice as large as the detrained liquid water from the ZM scheme (red line). The cloud liquid water is removed by production of precipitation (green line) and sedimentation of cloud droplets (brown line) that could be considered as drizzle. When the ZM scheme ceases to operate, the HK scheme becomes active; detrained liquid water from the HK scheme is then the main source of cloud water, while evaporation is the largest sink. If the detrained liquid from the shallow convection scheme is evaporated within the HK scheme instead of being passed to the stratiform process, its net effect on cloud liquid water and on water vapor is much smaller than that of ZM scheme. The liquid water budget averaged over a cycle in the cloud layer thus balances the source of stratiform condensation plus detrainment and the sink due to precipitation and sedimentation of cloud drops.

Therefore, the ZM scheme supplies the water vapor, which then causes large-scale condensation and, thus, cloud liquid water. The detrainment of liquid water plays a smaller role. Since detrainment in the ZM scheme occurs at the neutral buoyancy level, the detrained water vapor should not automatically result in condensation. This is however made possible because of the radiative cooling of the cloud layer. Figure 6d shows the temperature tendencies in the layer. When the ZM scheme is active, the radiative cooling (brown line), instead of being balanced by entrainment of warm air above the inversion, is balanced by heating from stratiform condensation (cyan line), large-scale forcing (green line), and convection (red line). The strong radiative cooling is due to the presence of cloud liquid water. An interesting question is how the liquid water is formed in the first place if there is no detrained liquid water. When water vapor is detrained, the relative humidity of the environment air rises. If it exceeds a threshold, stratiform clouds form and condensation takes place (Zhang et al. 2003). A similar process would occur in most statistical cloud schemes. In the present calculation, detrainment of liquid water from the ZM scheme also provides the seeds of liquid water.

The large contribution of stratiform condensational heating in the heat budget is somewhat puzzling. The radiative cooling does not prompt turbulence at the top of the cloud layer. Instead, it causes condensation that further feedbacks to the radiative cooling. This phenomenon could be very different in a model with explicit cloud-top entrainment parameterization based on radiative cooling of the cloud layer, such as used in Lock et al. (2000).

We now turn to the causes of the life cycle of clouds in the simulation. We focus on the ZM convection scheme since it is primarily responsible for the formation of the stratiform clouds in the simulation. Air parcels in the ZM scheme originate from the layer of maximum moist static energy in the boundary layer, which is always the lowest model layer in the simulation. Figure 7a shows two time snapshots of the vertical profiles of moist static energy and saturated moist static energy (h^*), one at day 42.3 when the ZM scheme is active (solid color) and one at day 42.6 when it is inactive (dashed color). The h^* at the initial time is also included in the figure as the black dotted line, which also indicates the deviation of the temperature profile from the initial equilibrium state without a PBL. The small variation of saturated moist static energy (h^*) from $t = 42.3$ to $t = 42.6$ suggests that temperature plays a small role in the variation of the vertical instability. The relatively large variation of the moist static energy (h) near the surface between the two times indicates that mois-

ture is the main contributor of the instability variation. While there is potential convective instability at all times, only when the lowest layer is sufficiently wet, and the total convective available potential energy (CAPE) is positive, can convection initiate in the ZM scheme. Moisture in the lowest model layer therefore regulates the ZM convection in the simulation.

The supply of lower level moisture is dominantly from the boundary scheme, as shown by the brown line in Fig. 7b before day 42. Once convection is triggered, convective subsidence and downdrafts lead to significant drying of the lowest layer (red line) that almost balance the turbulent moistening (brown line). This temporary balance, however, does not last long before the turbulent tendency weakens and suddenly becomes negative. The ZM convection then stops. It is activated in the next cycle when the turbulent moistening brings back the moisture into the lowest model layer.

The interplay between the boundary layer scheme and the ZM convection scheme can be more clearly seen in the vertical profiles of their moisture tendencies in Fig. 7c. The solid lines show the tendencies at day 42.3 when the ZM scheme is active. The ZM scheme (red) is associated with drying at and below 950 mb and moistening at 900 mb. The surface drying offsets the turbulent moistening. The dashed line shows the moisture tendency from the turbulent scheme at day 42.6 when the ZM convection is inactive. At this time, the PBL turbulence transports moisture upward to moisten the 950 mb layer. As shown in Fig. 7b, the PBL scheme actually dries the surface layer significantly in a short period of time, leading to the demise of the ZM convection at around day 42.5.

What causes the turbulent tendency of surface moisture in the PBL to become smaller and then switch sign in Fig. 7b? Turbulent diffusivities in the model are dependent on the boundary layer height. The boundary layer height is diagnostically calculated using a threshold bulk Richardson number with vertical interpolation in the CAM3 (Holtslag and Boville 1993). Because vertical profiles of winds are fixed, the bulk Richardson number depends on the vertical gradient of potential temperature. For most of the time, the height of the PBL in the simulation is below 975 mb, which is the bottom of the 950-mb layer, but it sometimes moves above the 950-mb altitude. The solid lines in Fig. 7d show the temperature tendency at 950 mb at day 42.3 (only tendencies from the ZM scheme and from the stratiform processes are shown here). It is seen that, when the ZM convection becomes active, there is a net cooling tendency of temperature in this layer (blue line). The source of the cooling is dominated by the evaporation of sedimenting cloud liquid in the strati-
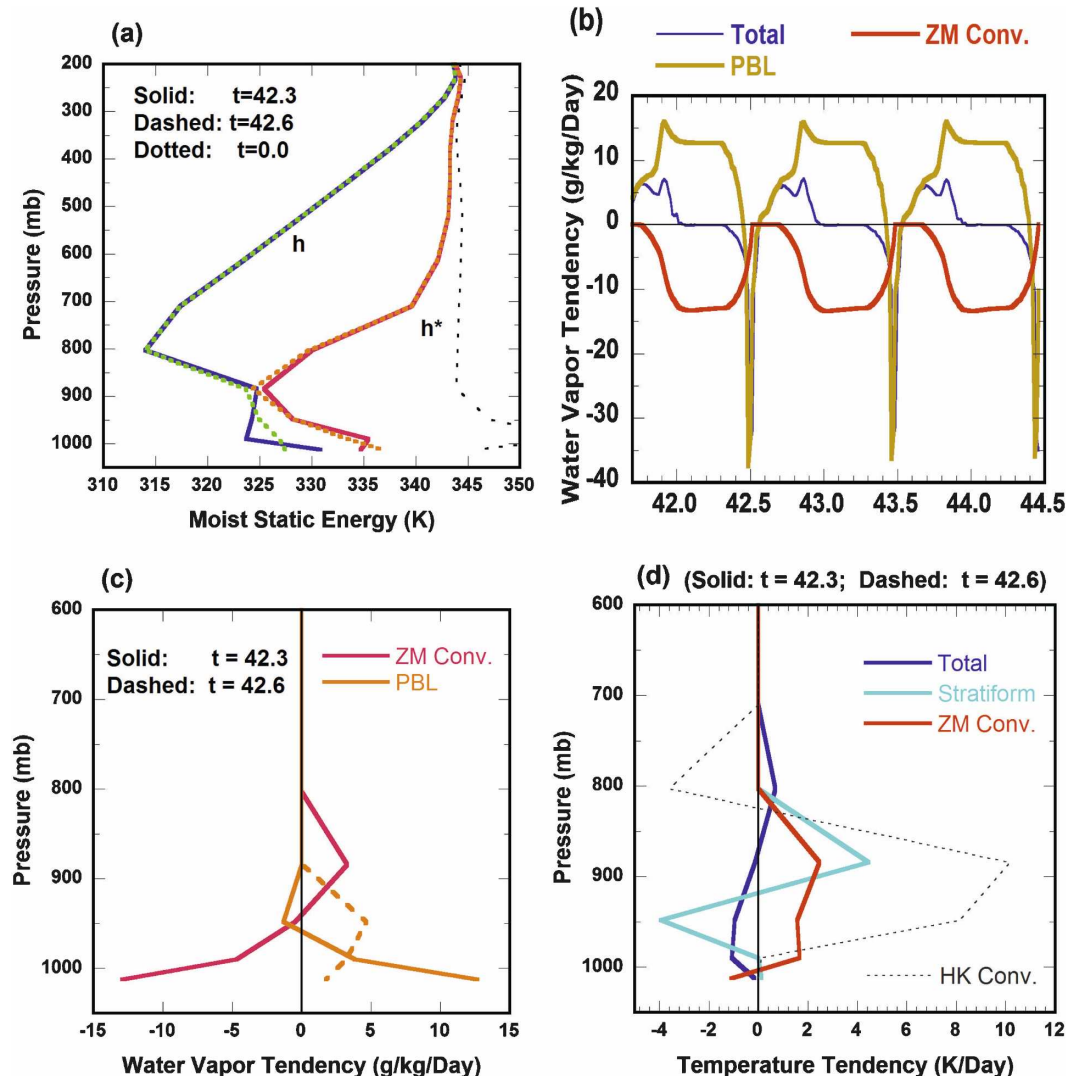
FIG. 7. (a) Profiles of moist static energy (*h*) and saturated moist static energy (*h**) at day 42.3 when the penetrative convection is active (solid lines) and at day 42.6 when it is inactive (dashed lines). The dotted black line is *h** at the initial time. (b) Time series of water vapor tendencies in the surface layer. As in (a) but for (c) water vapor and (d) temperature tendencies.

form cloud scheme, which was originated from the ZM convection scheme (cyan line) in the layer above. The evaporative cooling from rainfall is found to be relatively small. At this 950-mb level, the ZM convection scheme tends to warm the layer, but it is not sufficient to offset the evaporative and radiative cooling. As a result, temperature at 950 mb decreases monotonically when the ZM scheme is active, which causes the boundary to first gradually rise, and then suddenly penetrates to the layer at 950 mb.

The deepening of the boundary layer moistens the 950-mb model layer, but dries the surface layer. This shuts off the ZM convection scheme. While this process indirectly stabilizes the ZM scheme, the deepened PBL

provides sufficient moisture for the HK scheme to become active. This scheme causes subsidence warming of the 950-mb layer as shown by the thin dashed line in Fig. 7d for day 42.6. This warming compresses the depth of the boundary layer. Moisture near the surface then increases quickly from turbulent transport (Fig. 7b) for the penetrative convection to recover.

The maintenance of clouds in the control simulation is therefore the result of interaction of several parameterization components including the ZM and HK convection schemes, the stratiform cloud schemes, radiation, and the boundary layer scheme. The interactions are schematically summarized in Fig. 8 as two stages. The first stage (Fig. 8a) is characterized by the active
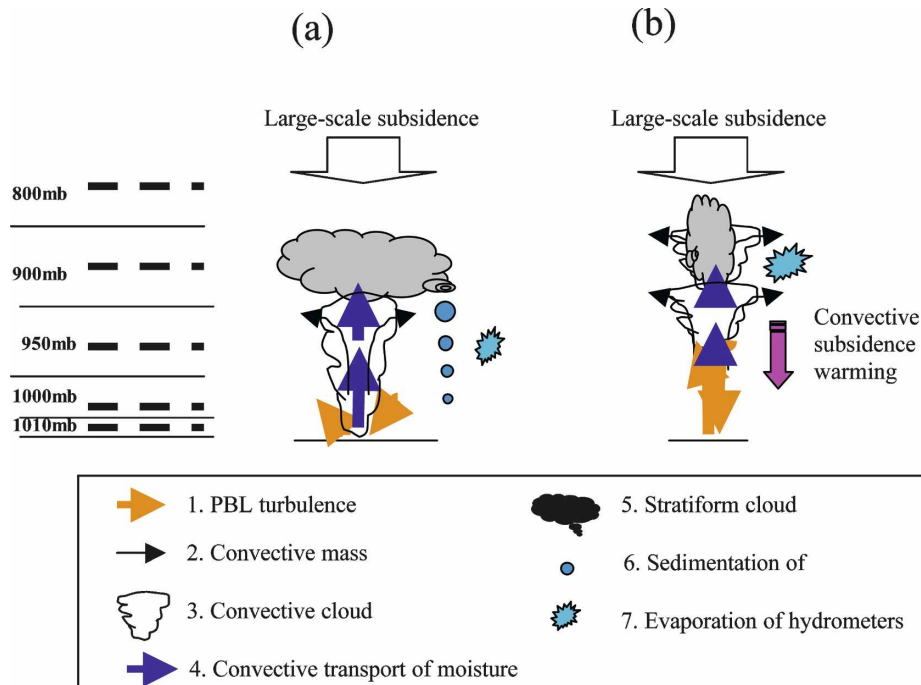
FIG. 8. Schematics of the interaction of the boundary layer scheme and penetrative as well as shallow convection. The approximate model midlevels (dashed lines) and the interface levels (solid lines) are shown at the left of the figure. The legend box at the bottom of the figure describes the symbols in (a): the symbols are arranged in order to facilitate the discussions in the text.

penetrative ZM convection. It has the following main features as described in order in the legend box at the bottom of the figure: (i) In the surface layer, the turbulent drying from upward transport of moisture is balanced by surface evaporation. (ii) Penetrative convection originates from the surface layer; associated with it are convective clouds and upward transport of moisture. (iii) Stratiform clouds form due to detrainment of moisture; the detrained water vapor from the ZM convection scheme and radiative cooling causes stratiform condensation and accumulation of cloud water at the detrainment level. (iv) Evaporative cooling below the detrainment layer from sedimentation cloud liquid, along with radiative cooling, causes temperature near the boundary layer top to decrease. This last feature causes the boundary layer to rise.

In the next stage (Fig. 8b), the boundary layer rises to a higher level. Its main features are (i) activation of the HK shallow convection scheme because of the moistening of the upper boundary layer from the PBL transport; (ii) net drying of the surface layer by the vigorous upward PBL transport in the deepened boundary layer, which causes the ZM scheme to stop; and (iii) warming and drying from the HK scheme at its cloud base around 950 mb. This last feature causes the PBL to become shallow. The ensuing surface evaporation then preconditions the activation of the ZM convection scheme in the next cycle. Once the ZM scheme is active, it dries up the moisture source for the shallow convection scheme to operate.

The above processes have some resemblance to the schematic interaction of shallow cumulus, stratocumulus, and boundary layer turbulence drawn from the Atlantic Stratocumulus Transition Experiment (ASTEX) (Albrecht et al. 1995; Miller and Albrecht 1995). These include the coupling of the surface with the stratocumulus layer through the ZM scheme, and the role of shallow cumulus in the decoupling of stratocumulus with the surface layer. The relative importance of the processes, however, is subject to great uncertainties in the model.

The above analysis also shows that in CAM3, cloud liquid water amount is not a simple function of temperature. Instead, it depends on the amount of detrained moisture and radiative cooling, influenced by a suite of processes. It also depends on the persistence time of the ZM convection.

b. Response of clouds to warmer climate

To more clearly illustrate the mechanism of cloud response to large-scale environment, we first fix the large-scale advective forcing of temperature and water
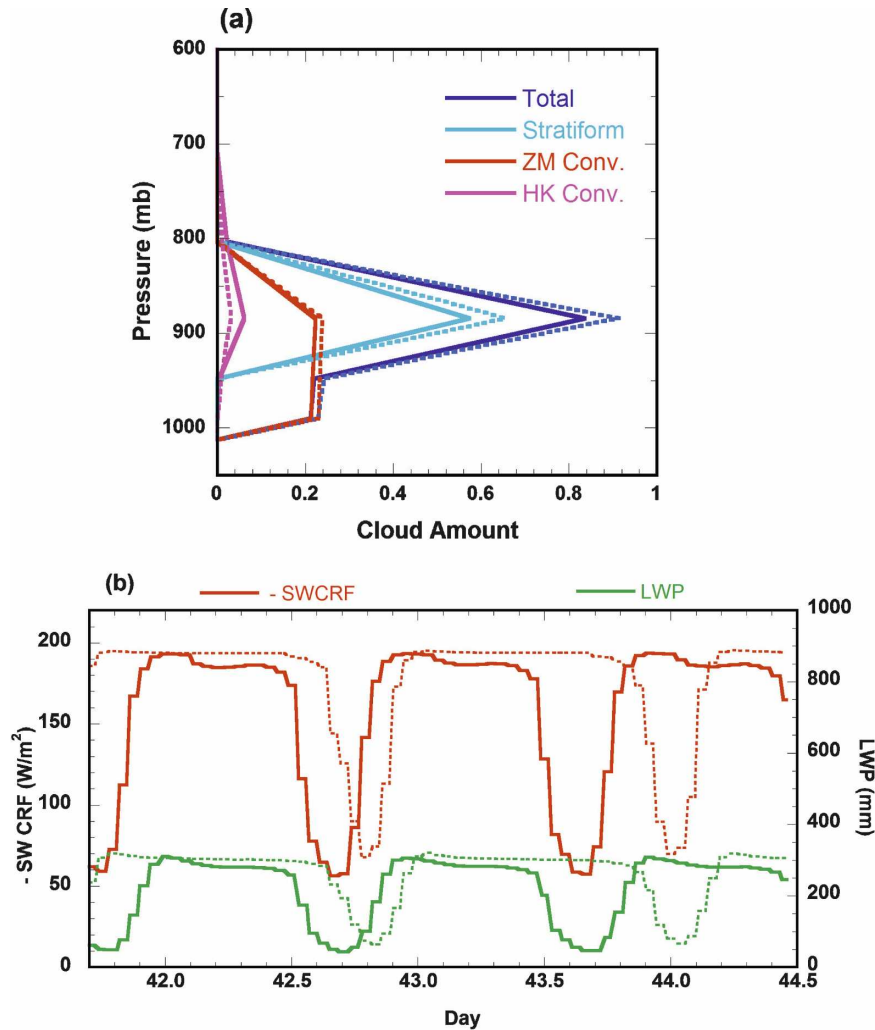
FIG. 9. (a) Profiles of cloud distributions in the warm simulation (dashed lines) and in the control simulation (solid lines). (b) Column-integrated cloud liquid water path and cloud shortwave cooling in the warm simulations (dashed lines) and in the control simulations (solid lines).

vapor as in the control case but raise the SST by 2°. The difference with the control simulation is therefore purely thermodynamic. The simulation shows quasi-periodic variation of clouds similar to the control case at about 900 mb, produced by the same interactions of processes. Figure 9a shows the time-averaged vertical profiles of convective and stratiform cloud amount in both the control (solid) and warm experiments (dashed).

The warm simulation has more low clouds, from both stratiform source and the ZM convection. Cloud production from the HK scheme is reduced, but convective clouds are not directly associated with liquid water in the model. A time segment of the comparison of the column cloud liquid water path is shown in Fig. 9b

(green lines). There is more cloud water in the warm simulation. Figure 9b also compares the shortwave cloud cooling (red lines) in the warm case with the control case. Cloud feedback is negative. This is consistent with results from the parent CAM3. It is, however, difficult to infer the physical mechanisms of the cloud feedback from the mean profiles in Fig. 9a.

Figure 9b suggests that two main features account for the larger shortwave cooling in the warmer case: 1) more cloud liquid when the penetrative convection scheme is active and 2) longer maintenance of the ZM convection.

The shortwave cloud feedback is -9 W m^{-2} K^{-1}. The absolute magnitude of this number should not be taken literally because of the perpetual conditions used.

About half of this feedback is contributed by the larger amount of liquid water when the penetrative convection is active. The remaining half is due to the longer persistence of the ZM convection that deposits moisture to the 900-mb layer. This partitioning is estimated by averaging the cloud forcing for times when the ZM scheme is active.

To understand the higher cloud liquid water content in the warm simulation, we use the red lines in Fig. 10a to show the water vapor concentration of the lowest model layer in the control case (solid) and perturbed case (dashed). As expected from the Clausius–Clapeyron equation, water vapor is increased with the rate of about 7% per degree of surface temperature (14% for 2°). The green lines in the figure compare the convective mass fluxes of the ZM scheme in the two simulations. It is seen that convective mass flux has increased by about the same percentage in the warm case. This increase can be explained by using the following CAPE measure after it is integrated to the neutral buoyancy level,

$$h_0 - h_z^* = (s_0 - s_z) + L(q_0 - q_z^*), \qquad (8)$$

where the subscripts "0" and "z" represent the surface layer and any layer at height z; the asterisk denotes saturation; s and q are dry static energy and water vapor concentration, respectively. The rate of CAPE change with surface temperature therefore is dominated by q_0. Since the mass flux is calculated based on CAPE divided by the rate of consumption of CAPE by a unit mass flux, which was found to be insensitive to temperature, the larger CAPE in the warm simulation corresponds to larger convective mass fluxes. Therefore, the dependence of the mass flux on surface temperature can be traced back to the Clausius–Clapeyron relation of moisture with temperature. This dependence is different in regions of deep convection that span the depth of the troposphere, where convective mass fluxes may decrease with surface temperature (Held and Soden 2006). The consumption of CAPE in the latter case is due to the warming of the troposphere, rather than the drying of the surface layer.

The larger mass flux, combined with a larger water vapor concentration, corresponds to a larger percent increase of upward water vapor transport. This is shown by the yellow lines in Fig. 10b. The stratiform condensation is about 14% larger in the warm simulation than in the control simulation, as shown by the blue lines, since it is determined by the relative humidity rather than the moisture content. The larger condensa-

tion leads to more cloud liquid water as shown in Fig. 10c. This contributes to the increase of shortwave cloud cooling or the negative cloud feedback.

To understand the longer period in the warm simulation, we examine why the burst of the boundary layer is delayed. As mentioned before, the temperature at the 950-mb layer regulates the PBL height in the simulation. The orange lines in Fig. 11a compares the convective warming of the ZM scheme due to subsidence in the two experiments at 950 mb. The percentage increase of the warming is similar to that of the convective mass flux. The cyan lines in Fig. 11a compare the evaporative cooling from sedimentation of cloud drops in the two cases. The percentage increase is much smaller. The net cooling at 950 mb is therefore weaker in the warm simulation. As a result, the deepening of the PBL is slowed.

The asymmetric change of the convective warming and evaporative cooling at 950 mb can be attributed to the efficient rainwater production in the model. The dependence of rainwater production from autoconversion is more than linear (Rasch and Kristjánsson 1998). The asymmetric sensitivities can be illustrated using the following idealized balance of condensation (C) and production of precipitation (P):

$$C = P. \qquad (9)$$

If P is parameterized as a function of cloud liquid water (l) as

$$P = \alpha l^\beta, \qquad (10)$$

where $\alpha > 0$ and $\beta > 1$, one can show that

$$\frac{\delta C}{C} = \frac{\delta P}{P} = \beta \frac{\delta l}{l}. \qquad (11)$$

Therefore, the percentage increase of the liquid water is smaller than that of the condensation and precipitation production. As a result, most of the increased condensation goes to enhance the production of precipitation rather than the cloud water. Cloud sedimentation is therefore only slightly larger (Fig. 11) in the warm simulation.

The slower deepening of the PBL prolongs the life cycle of the ZM convection, which contributed to the negative cloud feedback. The ZM convection also recovers faster after it is deactivated because of the larger moistening rate from surface evaporation in the warmer simulation.
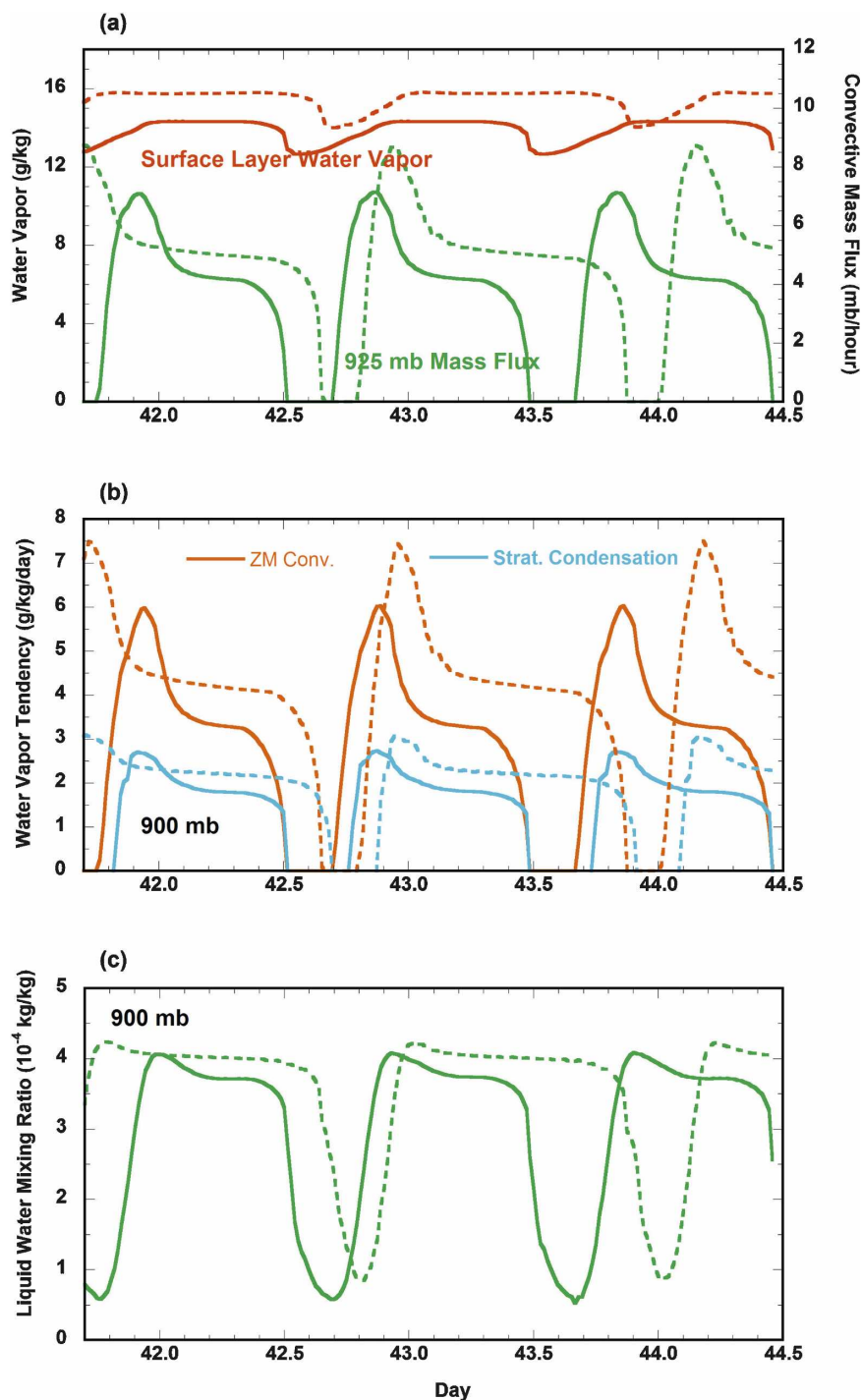
FIG. 10. (a) Water vapor mixing ratio at the 900-mb level and convective mass flux at 925 mb. (b) Tendency of water vapor from the penetrative convection scheme and stratiform condensation at the 900-mb level. (c) Liquid water mixing ratio at 900 mb. In all figures dashed lines are for the warm simulation; solid lines are for the control simulation.

Figure 12 shows a schematic of the negative cloud feedback from the above analysis. The magnitudes of the relative change of the physical processes are marked by the color coding described in the legend box at the bottom of the figure. The larger liquid water at the detrainment level and the smaller cooling at 950 mb ultimately contribute to the increased shortwave cloud cooling.
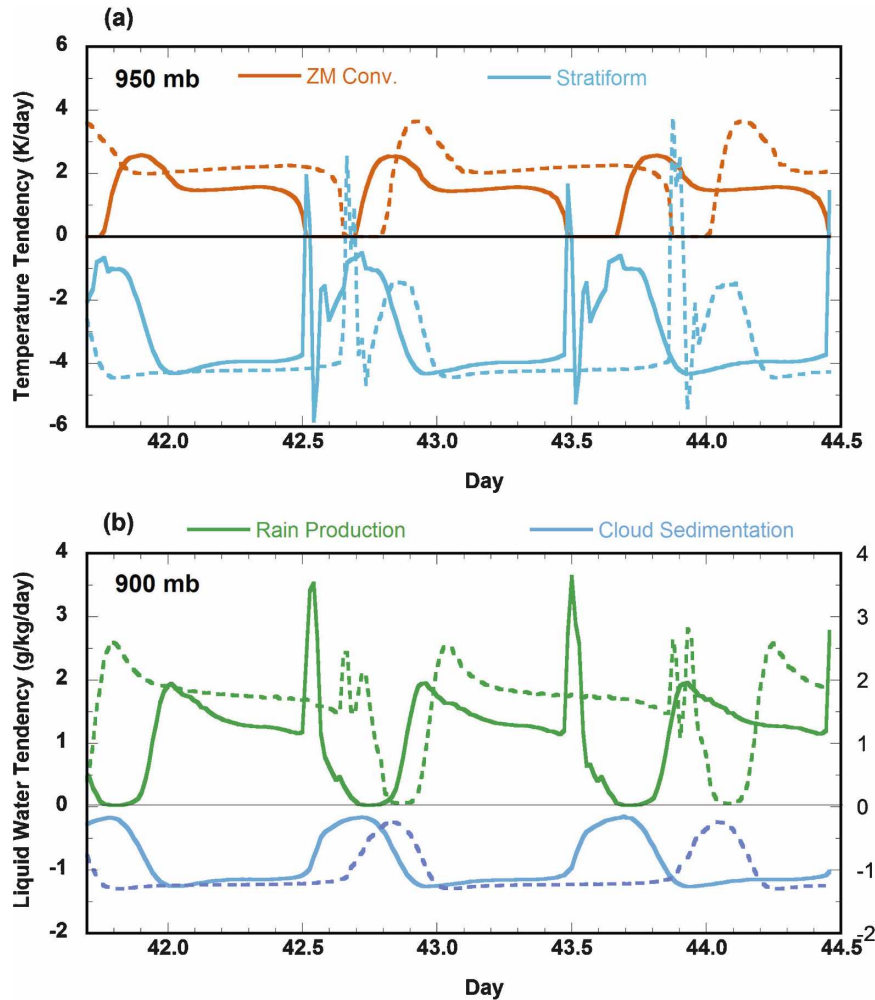
FIG. 11. (a) Temperature tendencies from the penetrative convection and from stratiform evaporation at the 950-mb level and (b) rainwater production and removal of cloud water by sedimentation. Dashed lines are for the warm simulation; solid lines are for the control simulation.

c. Response of clouds to dynamic forcing

We next add the weaker subsidence and the corresponding advective tendencies of temperature and water vapor as in the warm simulation. The results are compared with those in the previous subsection with fixed large-scale forcing. The difference is therefore due to the large-scale dynamics.

Figure 13a compares the time-averaged profiles of cloud amount (dashed lines) with that in the fixed forcing simulation (solid lines). Both convective and stratiform clouds are increased. Figure 13b compares the cloud liquid water (green lines) and the shortwave cloud cooling (red lines) in the two simulations. There is very little sensitivity of the cloud liquid change when the ZM convection is active, which can be understood from Eq. (11). The weaker subsidence, however, cor-

responds to more liquid water when averaged over the cycle because of more fractional clouds. It therefore has a larger shortwave cooling, thus negative cloud feedback. The magnitude of the negative cloud feedback from the weaker dynamic forcing is one quarter of that from the temperature alone. Table 1 gives the time-averaged cloud forcing from the three experiments. In the table, $\Delta\omega$ describes the interactive dynamics.

The additional negative cloud feedback from the interactive dynamics can be explained by the increased amount of convective mass fluxes in the simulation. Because the atmosphere with weaker subsidence is less stable than that with stronger subsidence, convective mass flux is increased (Fig. 14a). The reduced warming from large-scale subsidence (blue) is therefore accompanied by enhanced convective warming due to increased mass flux (Fig. 14b). Following the discussions
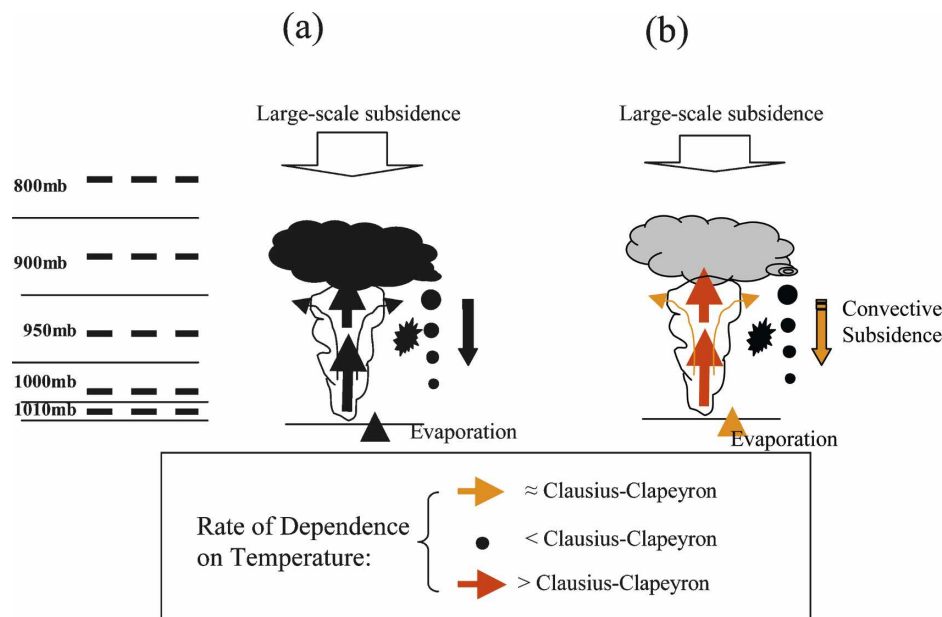
FIG. 12. Schematics of cloud feedbacks in the warm simulation: (a) the control simulation that corresponds to Fig. 8a and (b) The warm simulation with the variation of main components coded with color in the legend box as to be smaller than, equal to, or lager than the Clausius–Clapeyron percentage dependence of moisture on temperature. The negative feedback is due to more in-cloud liquid water and longer cloud lifetime.

in section 3b, the larger mass flux causes more condensation and thus a negative cloud feedback. Note that the period of the cloud variation is shorter in the simulation with weaker subsidence (Fig. 14b). This is consistent with the reduced large-scale subsidence warming that affects the PBL deepening. The period here, however, does not exert a large influence on the cloud feedback.

4. Summary and discussion

It is obvious that much can be done to expand investigations reported in this paper. These include sensitivities of the model results to specifications of control parameters such as the SSTs and to modified parameterizations. Applicability of the results from the idealized simulations to the parent GCM needs to be studied. The realism of the processes described in the previous section with respect to observations and large-eddy simulation is also of great interest. The importance of higher vertical resolution in describing low clouds has been emphasized in the literature (e.g., Emanuel and Zivkovic-Rothman 1999) and is consistent with intuition, although recent stratocumulus-capped boundary layer intercomparison studies suggest more sensitivity to physical parameterizations than to improved resolution (e.g., Zhu et al. 2007; Wyant et al.

2007). The implication of these results to the cloud feedback problem should be studied. These will be pursued elsewhere. Results from this paper can be summarized as follows:

1) Our idealized setup of large-scale forcing conditions has produced low-level cumulus and stratocumulus clouds in the CAM3. The setup also produced a negative cloud feedback from low clouds that is consistent with that in the climate change simulations of the GCM.

2) Low clouds are produced in the model because of the combined effects of detrainment of water vapor from penetrative convection, the production of condensates from the stratiform cloud scheme, and the radiative cooling of the cloud layer. In the model, the two convection schemes are responsible for most of the vertical moisture transport into the cloud layer and the entrainment through the trade inversion.

3) The life cycle of clouds is controlled by the interaction of convection with the boundary layer scheme: evaporation of sedimenting cloud droplets originating from the penetrative convection deepens the subcloud turbulent layer. This initiates shallow convection at its top. The warming from the shallow convection suppresses the boundary layer, allowing surface evaporation to precondition the next cycle
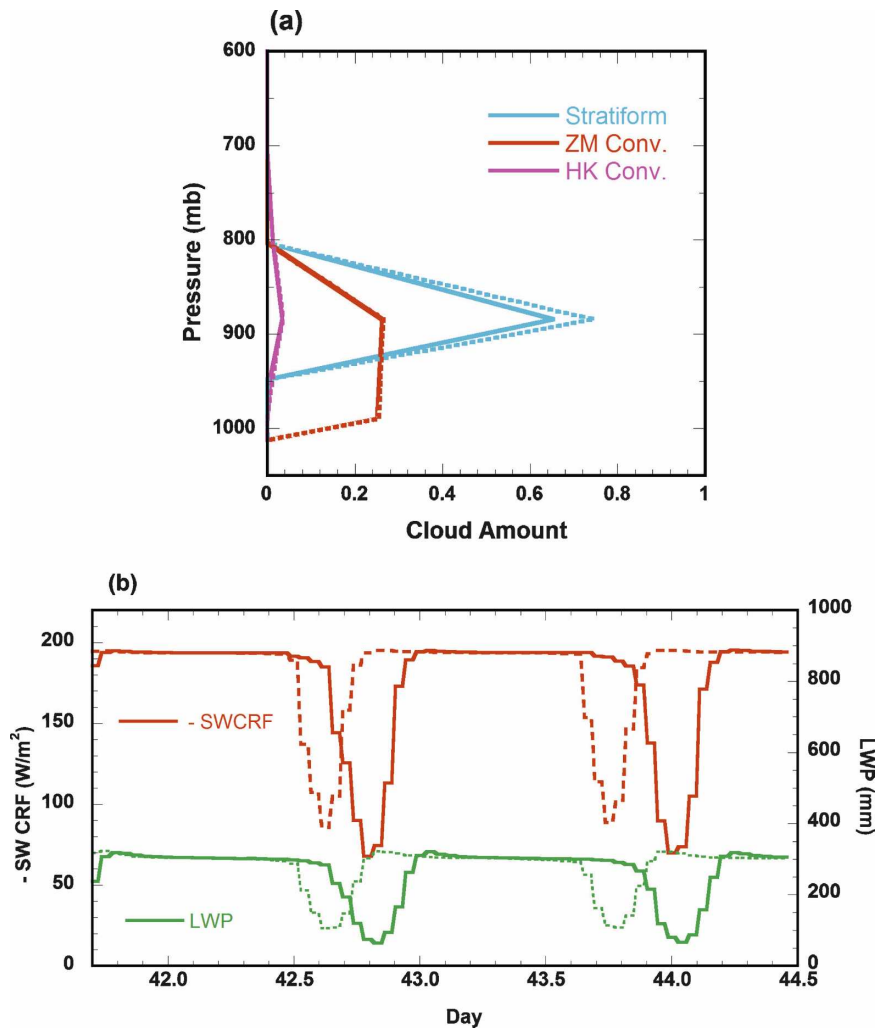
FIG. 13. (a) Profiles of time-averaged cloud distributions and (b) column-integrated cloud liquid water path and cloud shortwave cooling. Dashed lines are for the warm simulation with weaker subsidence; solid lines are for the warm simulation with fixed subsidence.

of penetrative convection. A schematic of these interactions was shown in Fig. 8.

4) The negative cloud feedback is produced by higher in-cloud liquid water content in stratiform clouds in a warmer climate. The higher liquid water concentration is due to larger detrainment of water vapor associated with a larger mass flux of shallow convection. The latter is further related to larger convective instability as a result of the Clausius–Clapeyron dependence of water vapor on surface temperature.

5) The longer lifetime of clouds in the simulation also contributes to the negative cloud feedback. The longer lifetime is due to a stronger temperature sensitivity of shallow convective mass flux than of liquid water concentration in stratiform clouds, which is limited by precipitation feedbacks. The increased mass flux leads to larger magnitude of convective warming than the cooling of sediment cloud droplets near the top of the boundary layer. This slows the deepening of the boundary layer; a deepened boundary layer tends to dry the surface layer, shut off the penetrative convection, and thus dissipate the clouds.

6) Weaker large-scale subsidence in the warmer cli-

TABLE 1. Simulated cloud forcing from the three experiments.

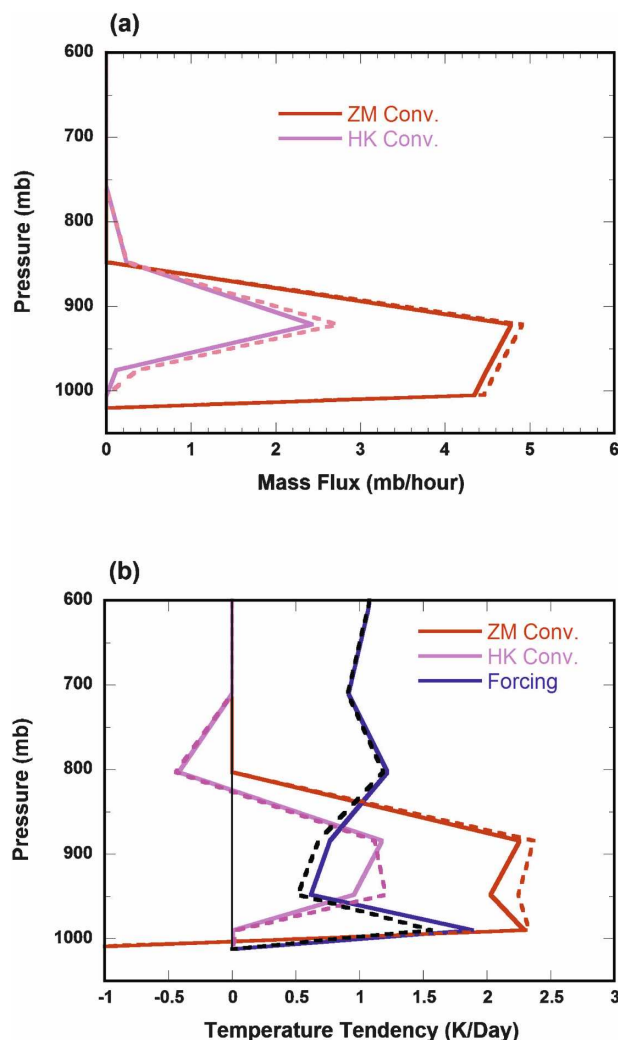| Mean CRF expt	SW CRF (W m^{-2})	LW CRF (W m^{-2})	Net CRF (W m^{-2})
Control	−155	13	−142
ΔSST = 2 K, Δω = 0	−173	14	−160
ΔSST = 2 K, Δω < 0	−179	14	−165

FIG. 14. Profiles of time-averaged (a) convective mass fluxes and (b) temperature tendencies. Dashed lines are for the warm simulation with weaker subsidence; solid lines are for the warm simulation with fixed subsidence.

mate corresponds to larger amount of convective mass fluxes, and thus more cloud water, causing a negative cloud feedback. The magnitude of the contribution of this dynamic effect, however, is only about one-quarter of the thermodynamic negative cloud feedback.

Our study shows the need to treat model physical parameterizations as an interactive system, not just as separate individual components. Our analysis procedure also illustrates the need to understand the maintenance of simulated clouds in the basic climate in order to fully understand the sensitivity of these clouds to a climate change. Zhang et al. (2005) compare simulated clouds in nine contemporary GCMs with satellite

measurements by using an International Satellite Cloud Climatology Project (ISCCP) simulator in all these models. They revealed substantial differences of model clouds with observations, suggesting that GCMs may not be maintaining subtropical boundary layer clouds through the correct balance of physical processes.

One might imagine from this study that the low cloud response to climate change should be very sensitive to parameterization changes in CAM. Surprisingly, so far we have found the opposite. We tried a sensitivity study in which we reran the above simulations without the ZM scheme, so only the Hack shallow convection scheme (which is, in spirit, like a moist layer turbulence scheme with entrainment) is operative. The cloud thickens and lasts longer as the climate warms, though the detailed mechanism is a bit different. A newer version of CAM with quite different formulations of moist turbulence and shallow cumulus parameterizations following Bretherton et al. (2004) also has surprisingly similar subtropical low cloud feedbacks to CAM3 (Zhu et al. 2007). We intend to use the protocol in our current paper to understand whether there is a fundamental reason for these results.

Our simulations point to several issues broadly relevant to understanding low cloud feedbacks. First, the time-mean liquid water and cloud fraction are determined by the interaction of several physical processes, all with different responses to a climate perturbation. No one parameterization is dominating the cloud feedbacks. The parameterization components typically interact on the model grid scale. In reality, however, they interact mostly at the subgrid scales. For example, radiative cooling from clouds in climate models is applied to the whole model grid box in an entire model layer. This can prompt large-scale condensation rather than cloud-top entrainment of warm and dry air above the clouds. Even though some parameterizations explicitly calculate the cloud-top entrainments (Lock et al. 2000; GFDL Global Atmospheric Model Development Team 2004), the applied radiative cooling responsible for the entrainments is still a grid-scale variable.

Second, both precipitation/droplet sedimentation processes and the parameterizations responsible for entraining air from above the trade inversion (the cumulus parameterizations, in our case) play an important role in determining the simulated mean cloud properties. Whether precipitation processes are important for low cloud feedbacks in reality is an open question, but they certainly are for our simulations and probably in many other GCMs. In particular, our results suggest that cumulus-cloud microphysics, which is often parameterized in an extremely oversimplified way, may be

contributing to GCM-simulated low-cloud climatology and the response to climate change.

Last but not least, the change of cloud amount with temperature is an interesting question. In the present case, low cloud processes are driven by convection. The convective mass flux increases with surface temperature approximately following the Clausius–Clapeyron relationship. The upward convective transport of water vapor therefore increases with temperature at roughly double this rate. Relative humidity then increases, and so does the cloud amount as a result of radiative cooling of the cloud layer. The dependence of cloud amount on temperature is therefore the result of the full suite of physical parameterizations in the model, which should be understood in the context of the first principles of the model physics.

REFERENCES

Albrecht, B. C., M. P. Jensen, and W. J. Syrett, 1995: Marine boundary structure and fractional cloudiness. *J. Geophys. Res.,* **100,** 14 209–14 222.

Bony, S., and J.-L. Dufresne, 2005: Marine boundary layer clouds at the heart of tropical cloud feedback uncertainties in climate models. *Geophys. Res. Lett.,* **32,** L20806, doi:10.1029/2005GL023851.

——, and Coauthors, 2006: How well do we understand and evaluate climate change feedback processes? *J. Climate,* **19,** 3445–3482.

Bretherton, C. S., R. Ferrari, and S. Legg, 2004: Climate Process Teams: A new approach to improving climate models. *U.S. CLIVAR Variations,* **2** (1), 1–6.

Caldwell, P., and C. S. Bretherton, 2008: Response of a subtropical stratocumulus-capped mixed layer to climate and aerosol changes. *J. Climate,* in press.

Cess, R. D., and Coauthors, 1990: Intercomparison and interpretation of climate feedback processes in 19 atmospheric general circulation models. *J. Geophys. Res.,* **95,** 16 601–16 615.

Clement, A., and R. Seager, 1999: Climate and the tropical oceans. *J. Climate,* **12,** 3383–3401.

Collins, W. D., and Coauthors, 2006: The Community Climate System Model Version 3 (CCSM3). *J. Climate,* **19,** 2122–2143.

Del Genio, A. D., W. Kovari, M.-S. Yao, and J. Jonas, 2005: Cumulus microphysics and climate sensitivity. *J. Climate,* **18,** 2376–2387.

Emanuel, A. K., and M. Zivkovic-Rothman, 1999: Development and evaluation of a convection scheme for use in climate models. *J. Atmos. Sci.,* **56,** 1766–1782.

GFDL Global Atmospheric Model Development Team, 2004: The new GFDL Global Atmosphere and Land Model AM2–LM2: Evaluation with prescribed SST simulations. *J. Climate,* **17,** 4641–4673.

Hack, J. J., 1994: Parameterization of moist convection in the National Center for Atmospheric Research Community Climate Model (CCM2). *J. Geophys. Res.,* **99,** 5551–5568.

——, B. A. Boville, B. P. Briegleb, J. T. Kiehl, P. J. Rasch, and D. L. Williamson, 1993: Description of the NCAR Community Climate Model (CCM2). Tech. Rep. NCAR/TN-382+STR, National Center for Atmospheric Research, 120 pp.

Hansen, J., and Coauthors, 1984: Climate sensitivity: Analysis of feedback mechanisms. *Climate Processes and Climate Sensitivity,* J. E. Hansen and T. Takahashi, Eds., Maurice Ewing Series, Vol. 5, Amer. Geophys. Union, 130–163.

Held, I. M., and B. J. Soden, 2006: Robust responses of the hydrological cycle to global warming. *J. Climate,* **19,** 5686–5699.

Holtslag, A. A. M., and B. A. Boville, 1993: Local versus nonlocal boundary-layer diffusion in a global climate model. *J. Climate,* **6,** 1825–1842.

Kiehl, J. T., and P. R. Gent, 2004: The Community Climate System Model, Version 2. *J. Climate,* **17,** 3666–3682.

——, J. J. Hack, G. B. Bonan, B. A. Boville, D. L. Williamson, and P. J. Rasch, 1998: The National Center for Atmospheric Research Community Climate Model: CCM3. *J. Climate,* **11,** 1131–1149.

——, C. A. Shields, J. J. Hack, and W. D. Collins, 2006: The climate sensitivity of the Community Climate System Model: CCSM3. *J. Climate,* **19,** 2584–2596.

Klein, S. A., and D. L. Hartmann, 1993: The seasonal cycle of low stratiform clouds. *J. Climate,* **6,** 1587–1606.

Larson, K., D. Hartmann, and S. Klein, 1999: The role of clouds, water vapor, circulation, and boundary layer structure in the sensitivity of the tropical climate. *J. Climate,* **12,** 2359–2374.

Le Treut, H., Z. X. Li, and M. Forichon, 1994: Sensitivity of the LMD general circulation model to greenhouse forcing associated with two different cloud water parameterizations. *J. Climate,* **7,** 1827–1841.

Lock, A. P., A. R. Brown, M. R. Bush, G. M. Martin, and R. N. B. Smith, 2000: A new boundary layer mixing scheme. Part I: Scheme description and single-column model tests. *Mon. Wea. Rev.,* **128,** 3187–3199.

McClatchey, R. A., R. W. Fenn, J. E. A. Selby, F. E. Voltz, and J. S. Garing, 1972: Optical properties of the atmosphere. AFCRL-72-0497, 108 pp. [NTIS-AD753075.]

Miller, M. A., and B. A. Albrecht, 1995: Surface-based observations of mesoscale cumulus–stratocumulus interaction during ASTEX. *J. Atmos. Sci.,* **52,** 2809–2826.

Miller, R., 1997: Tropical thermostats and low cloud cover. *J. Climate,* **10,** 409–440.

Miura, H., H. Tomita, T. Nasuno, S. Iga, M. Satoh, and T. Matsuno, 2005: A climate sensitivity test using a global cloud resolving model under an aqua planet condition. *Geophys. Res. Lett.,* **32,** L19717, doi:10.1029/2005GL023672.

Moorthi, S., and M. J. Suarez, 1992: Relaxed Arakawa–Schubert: A parameterization of moist convection for general circulation models. *Mon. Wea. Rev.,* **120,** 978–1002.

Randall, D. A., and Coauthors, 2007: Climate models and their evaluation. *Climate Change 2007: The Physical Sciences Basis,* S. Solomon et al., Eds., Cambridge University Press, 633–640.

Rasch, P. J., and J. E. Kristjánsson, 1998: A comparison of the CCM3 model climate using diagnosed and predicted condensate parameterizations. *J. Climate,* **11,** 1587–1614.

Senior, C. A., and J. F. B. Mitchell, 1993: Carbon dioxide and climate: The impact of cloud parameterization. *J. Climate,* **6,** 5–21.

——, and ——, 1996: Cloud feedbacks in the unified UKMO unified model. *Climate Sensitivity to Radiative Perturbations, Physical Mechanism and Their Validation,* H. Le Treut, Ed., Springer, 191–202.

Soden, B. J., and I. M. Held, 2006: An assessment of climate feedbacks in coupled ocean–atmosphere models. *J. Climate,* **19,** 3354–3360.

——, A. J. Broccoli, and R. S. Hemler, 2004: On the use of cloud forcing to estimate cloud feedback. *J. Climate,* **17,** 3661–3665.

Solomon, S., D. Qin, M. Manning, M. Marquis, K. Averyt, M. M. B. Tignor, H. L. Miller Jr., and Z. Chen, Eds., 2007: *Climate Change 2007: The Physical Sciences Basis.* Cambridge University Press, 996 pp.

Somerville, R. C. J., and L. A. Remer, 1984: Cloud optical thickness feedbacks in the CO_2 climate problem. *J. Geophys. Res.,* **89,** 9668–9672.

Stephens, G. L., 2005: Cloud feedbacks in the climate system: A critical review. *J. Climate,* **18,** 237–273.

Vecchi, G. A. B. J. Soden, A. T. Wittenberg, I. M. Held, A. Leetmaa, and M. J. Harrison, 2006: Weakening of tropical Pacific atmospheric circulation due to anthropogenic forcing. *Nature,* **441,** 73–76.

Webb, M. J., and Coauthors, 2006: On the contribution of local feedback mechanisms to the range of climate sensitivity in two GCM ensembles. *Climate Dyn.,* **27,** 17–38.

Wetherald, R. T., and S. Manabe, 1988: Cloud feedback processes in general circulation models. *J. Atmos. Sci.,* **45,** 1397–1415.

Wyant, M. C., C. S. Bretherton, J. T. Bacmeister, J. T. Kiehl, I. M. Held, M. Z. Zhao, S. A. Klein, and B. J. Soden, 2006a: A comparison of tropical cloud properties and responses in GCMs using mid-tropospheric vertical velocity. *Climate Dyn.,* **27,** 261–279.

——, M. Khairoutdinov, and C. S. Bretherton, 2006b: Climate sensitivity and cloud response of a GCM with a superparameterization. *Geophys. Res. Lett.,* **33,** L06714, doi:10.1029/2005GL025464.

——, and Coauthors, 2007: A single column model intercomparison of a heavily drizzling stratocumulus-topped boundary layer. *J. Geophys. Res.,* **112,** D24204, doi:10.1029/2007JD008536.

Zhang, G. J., and N. A. McFarlane, 1995: Sensitivity of climate simulations to the parameterization of cumulus convection in the Canadian Climate Centre general circulation model. *Atmos.–Ocean,* **33,** 407–446.

Zhang, M., 2004: Cloud-climate feedback: How much do we know? *Observation, Theory, and Modeling of Atmospheric Variability,* X. Zhu et al., Eds., World Scientific Series on Meteorology of East Asia, Vol. 3, World Scientific Publishing, 161–183.

——, and H. Song, 2006: Evidence of deceleration of atmospheric vertical circulation over the Tropical Pacific. *Geophys. Res. Lett.,* **33,** L12701, doi:10.1029/2006GL025942.

——, J. J. Hack, J. T. Kiehl, and R. D. Cess, 1994: Diagnostic study of climate feedback processes in atmospheric general circulation models. *J. Geophys. Res.,* **99,** 5525–5537.

——, W. Lin, C. B. Bretherton, J. J. Hack, and P. J. Rasch, 2003: A modified formulation of fractional stratiform condensation rate in the NCAR Community Atmosphere Model (CAM2). *J. Geophys. Res.,* **108,** 4035, doi:10.1029/2002JD002523.

——, and Coauthors, 2005: Comparing clouds and their seasonal variations in 10 atmospheric general circulation models with satellite measurements. *J. Geophys. Res.,* **110,** D15S02, doi:10.1029/2004JD005021.

Zhu, P., J. T. Kiehl, J. J. Hack, and C. S. Bretherton, 2007: Climate sensitivity of tropical and subtropical marine low cloud amount to ENSO and global warming due to doubled CO_2. *J. Geophys. Res.,* **112,** D17108, doi:10.1029/2006JD008174.